Fluent Project 2

Ahijit Banerjee

November 23, 2022

1 Introduction

The purpose of the project is to analyze the lift and drag behaviour of the EPPLER 420 airfoil using ANSYS Fluent. We will be using the density-based solver and a turbulent model to study the effect of different angles of attack on the lift and drag coefficients across free-stream velocities ranging from $Ma = 0.3$ to $Ma = 0.9$. We intend to compare the results with the inviscid thin airfoil theory to understand how viscous models differ from it.

2 Materials and Methods

2.1 Global Settings

The settings that are not modified across simulation setups are referred to here as the global settings. They are listed below, the values that have not been explicitly stated have been left as the default values:

- Solver: Density Based
- Models: $k - \omega$ STT turbulence model, Energy On
- Materials: Air, set density as an ideal gas
- Boundary Conditions:

  Inlet, Bottom, Top-wall: Pressure far-field; $T = 273K$; $P = 0atm$;

  Outlet: Pressure-outlet; $T = 273K$; $P = 0atm$;

  Airfoil boundary: $T = 300K$

  Operating Conditions: $Pressure = 59607.1Pa$
- Reference Values: Ensure area is set to $1m^2$
- Methods: All implicit second-order methods in space
- No Convergence criteria set
- Enable report definitions for the coefficient of lift and drag report

2.2 Varying Angle of Attack

The regular operations of an airfoil involve changing its angle of attack to modulate its lift-to-drag ratio to control the operations of the aircraft. In this section, we will be modifying the airfoil's angle of attack by changing the direction of the incident freestream velocity. The angle of attack of the incident freestream is modified by changing the direction components of all three "pressure-farfield" surfaces using the X and Y components mentioned in Table 1.

The coefficient of lift and drag are defined with respect to the direction of the free stream velocity, thus when we rotate the free stream to achieve an angle of attack, we must also rotate our lift and drag direction vectors. Lift is defined perpendicular to the direction of the free stream velocity whereas drag is defined in the direction of the free stream velocity. Thus, we're using the values specified in Table 1 to correct the direction of our lift and drag vectors.

Table 1: Component Vectors for Angle of Attack, Coefficient of Lift and Drag

Angle of Attack	**Inlet and Drag**		**Lift**	
	X-Component	Y-Component	X-Component	Y-Component
0°	1.0000	0.0000	0.0000	1.0000
2°	0.9994	0.0349	-0.0349	0.9994
4°	0.9976	0.0698	-0.0698	0.9976
8°	0.9903	0.1392	-0.1392	0.9903
15°	0.9659	0.2588	-0.2588	0.9659

2.3 Steady Case Simulations

2.3.1 AoA 0°, AoA 2°and AoA 4°($Ma = 0.3$)

The simulations for the angle of attacks of 0°, 2°and 4°at $Ma = 0.3$ were performed using hybrid initialization with a Courant number of 50 for 10000 iterations. The results steadied out around the 7000 iteration mark, but a buffer was kept to reconfirm solution stability.

2.3.2 AoA 8°($Ma = 0.3$)

The simulation was run using hybrid initialization. The first 2000 iterations were run using a Courant number of 5 to facilitate the process of resolving the turbulence in the flow, the Courant number was then increased to 50 for the next 1000 iterations followed by increasing the Courant number to 100 for the last 25000 iterations.

2.3.3 AoA 4°($Ma = 0.9$)

The simulation at $Ma = 0.9$ could not be initialized using hybrid initialization as there were sections of the mesh that did not have an initial condition. Consequently, standard initialization was used with the velocity inlet condition over the entire flow. A Courant number of 0.5 was used for the first 2000 iterations, thereafter the Courant number was increased to 15 for the next 15000 iterations. Observing that the results were now changing slowly, the Courant number was increased to 75 for the last 10000 iterations.

2.4 Unsteady Case Simulation

The unsteady simulation for an angle of attack of 15°at $Ma = 0.3$ was initialized using the steady case solution. The steady case solution was obtained by using standard initialization and a Courant number of 1 for 500 iterations followed by 1500 iterations at a Courant number of 50. The Courant number for the unsteady simulation was also set to 50. The simulation was switched to a transient one from the "General" tab, in the "Methods" an implicit second-order temporal scheme was used along with the aforementioned implicit second-order spatial scheme.

If we had an explicit solver, we would have to limit our CFL number to 1 and therefore our time-step would be:

$$\Delta t = \frac{\Delta x}{u} \tag{1}$$

Since our velocity is nearly $100m/s$ and our grid size is of the order of 10^{-6}, our time-step would be around 10^{-8}. Fortunately, while using an implicit second-order time scheme we can increase the Courant number and our time-step without risking solution stability, although we need to be cautious that our time-step is small enough to capture the perturbations in the flow. We choose the time step to be $0.001s$ for 1000 iterations to simulate the results for a total of $1sec$ of flow. The process of selecting the time step is discussed later in the report.

3 Results and Discussion

3.1 Steady Solution at $Ma = 0.3$

On running the steady simulations for angles of attack 2°, 4°and 8°we observe the following trends in C_L, C_D and $\frac{C_L}{C_D}$ reported in Table 2. The results were obtained by averaging the reported values for the last 1000 iterations of the simulation.

Table 2: C_L, C_D and $\frac{C_L}{C_D}$ values for steady case simulations with varying angles of attack

AoA	C_L	C_D	$\frac{C_L}{C_D}$
2°	1.332174219570250	0.02257603300715138	59.00833946992631
4°	1.530532059940491	0.02460718957832067	62.19857229404671
8°	1.794295473379369	0.03906990625243728	45.92525668697851

Visualizing the trend of C_L and C_D with the angle of attack we observe that both the coefficient of drag and lift increase with the angle of attack in Figure 1. But the ratio of $\frac{C_L}{C_D}$ decreases resulting in an overall decrease in the performance of the airfoil.

Inviscid thin airfoil theory describes the change in C_L with the angle of attack using equation 2, where $C_{L_{\alpha=0}}$ is the coefficient of lift when the angle of attack is zero for cambered airfoils like the EPPLER 420. We observe that according to the thin inviscid airfoil theory, the slope of the C_L vs AoA plot is 2π.

$$C_L = 2\pi\alpha + C_{L_{\alpha=0}} \tag{2}$$

Thin airfoil theory uses the following assumptions that must be fulfilled to ensure a good quality approximate solution.

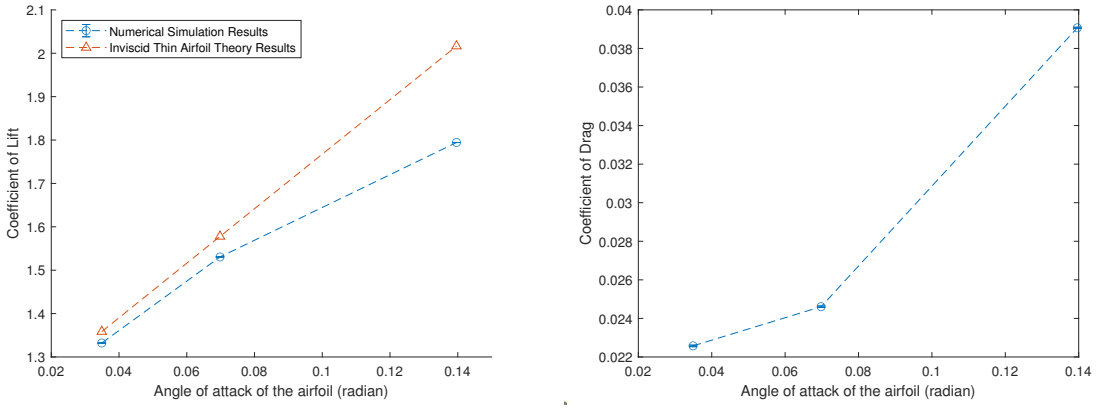

(a) C_L vs AoA

(b) C_D vs AoA

Figure 1: Plot of C_L and C_D vs Angle of Attack.

- Airfoil is asymptotically thin
- Camber is close to the chord
- AoA and camber are small
- Potential and incompressible flow

We observe from Figure 1 that our slope is 4.322247. The deviation in results from those described by the thin airfoil theory are due to the violation of the aforementioned assumptions that went into forming the simplified model. Our airfoil can be considered to be thin thereby satisfying the first two assumptions, but the last two assumptions are violated at higher angles of attack. When the angle of attack is increased both the small angle approximation and the potential, incompressible flow assumption breaks down as we start seeing flow seperation and an increase in vorticity in the wake of the airfoil. Consequently, we observe an decrease in our values of C_L and an increase in our value of C_D, reducing the overall performance of the airfoil compared to what thin airfoil theory predicted.

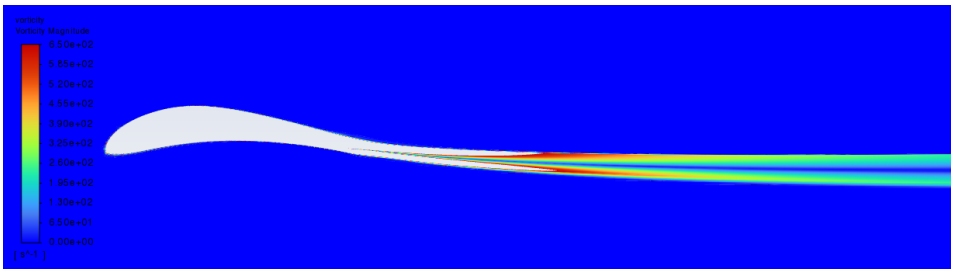

(a) Angle of Attack 2°

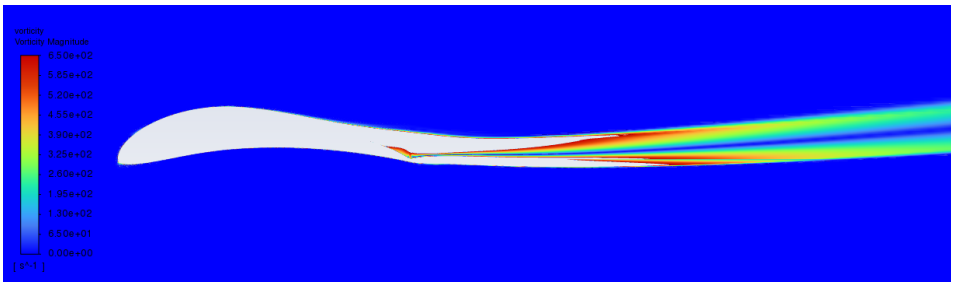

(b) Angle of Attack 8°

Figure 2: Vorticity Contour for different Angle of Attack

Observing the vorticity contours in Figure 2, we notice an increase in vorticity near the tail of

the airfoil for a higher angle of attack. The two contours are made on the same scale to facilitate comparison. In the angle of attack 8°contour, the $650s^{-1}$ starts noticeably later and is angled off towards the bottom. The increase in vortices for a higher angle of attack follows our initial conclusion that increasing the angle of attack would increase the vorticity and thus result in flow separation that would not have been captured by the inviscid airfoil results.

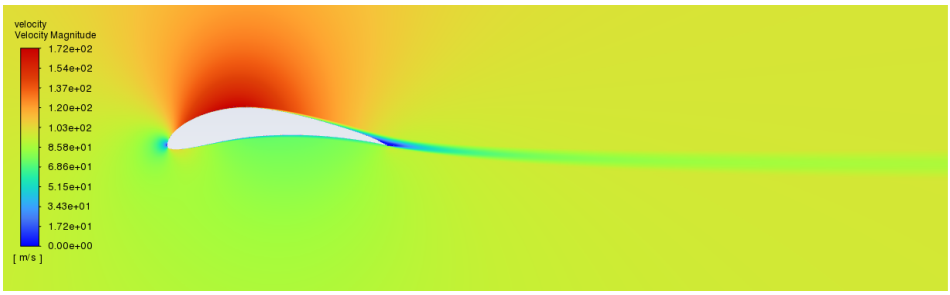

(a) Angle of Attack 2°

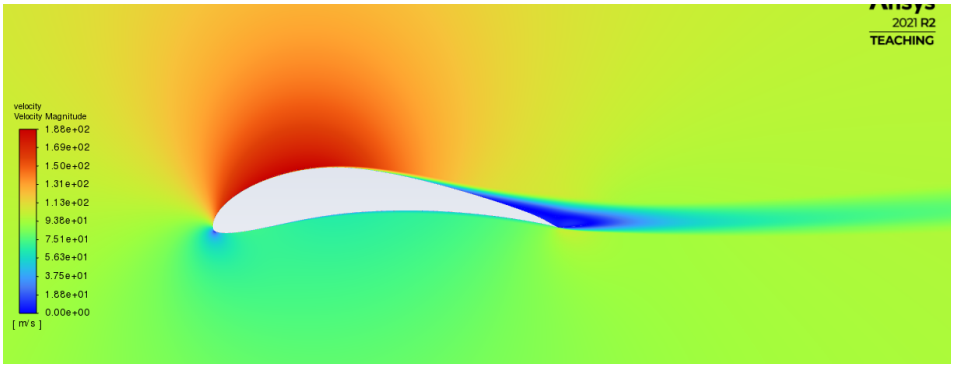

(b) Angle of Attack 8°

Figure 3: Velocity Contour for different Angle of Attack

On comparing the velocity contours for angles of attack of 2°and 8°respectively in Figure 3, we observe that at higher angles of attack the velocity of the air flowing over the airfoil is significantly higher than the velocity of the air on the lower surface of the airfoil. Since velocity and pressure have an inverse relationship from Bernoulli's principle, we know that there would be a low-pressure zone above the airfoil and a comparatively high-pressure zone below the airfoil, thereby creating a net lift force. The results obtained here do agree with the general trend observed in the inviscid airfoil theory that higher angles of attack would experience a higher lift force due to a larger difference in velocity in the air flowing over the two surfaces of the airfoil.

3.2 Steady Solution at $Ma = 0.9$

The C_L and C_D values for the EEPLER 420 airfoil with an angle of attack of 4°in a flow of $Ma = 0.9$ is 3.729501761221448 and 2.575458434901729 respectively.

In this case, we observe a shock wave forming predominantly on the top surface of the airfoil as the near sonic freestream accelerates to a supersonic flow due to the geometry of the airfoil. The shock wave is shown as the red wave in the velocity plot in Figure 4.

A shock wave causes sudden changes in fluid properties and is treated like a discontinuity in the flow. In this case, we observe an increase in the value of C_D from what we saw in the $Ma = 0.3$ case. The increase in drag can be attributed to the presence of the shock wave which introduces wave

Figure 4: Velocity Contour for Angle of Attack 4°

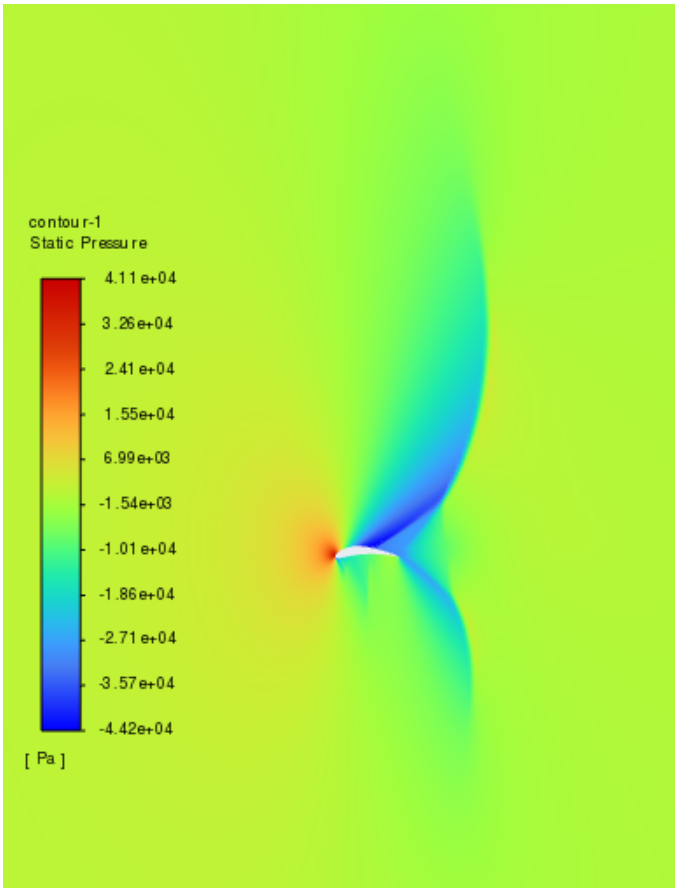

Figure 5: Pressure Contour for Angle of Attack 4°

drag alongside the viscous drag normally experienced by the airfoil. The shock wave also causes an overall increase in boundary layer separation.

The mesh used in the simulation was designed to provide higher resolution solutions for low angles of attacks. We can infer this from the resolution of the grid in the $-X$ direction behind the airfoil. But while running the various cases, we observe that the wake of the airfoil isn't always inline with the $-X$ direction depending on the angle of attack, thus creating a higher resolution mesh for a wider fan angle behind the airfoil will help. Furthermore, for near sonic cases where

we observe shock formations on the top surface of the airfoil which are hard to resolve due to the sudden discontinuities in the properties of the flow. For such cases providing a more resolved mesh on the top surface of the airfoil will help resolve any shocks that may form.

3.3 Unsteady Solution at $Ma = 0.3$

The primary observation for the high angle of attack case is the vortex shedding observed behind the airfoil. The vorticity contours are shown at time $t = 0$ and time $t = 1sec$ in Figure 6, and we can observe the vortex shedding in the wake of the airfoil. The value of $\frac{C_L}{C_D}$ for an angle of attack of 15°drops from close to 60 for lower angles of attack to about $10 - 20$. The drastic reduction in the value of $\frac{C_L}{C_D}$ shows a severe loss in performance of the airfoil and a potential risk for stalling.

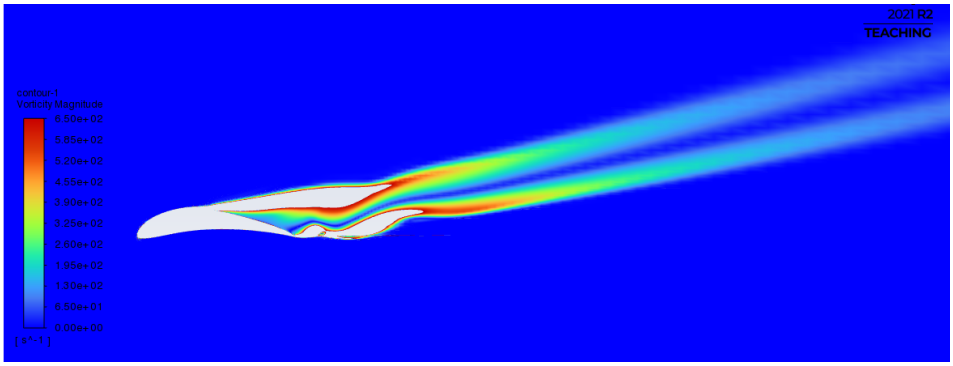

(a) Time = 0s

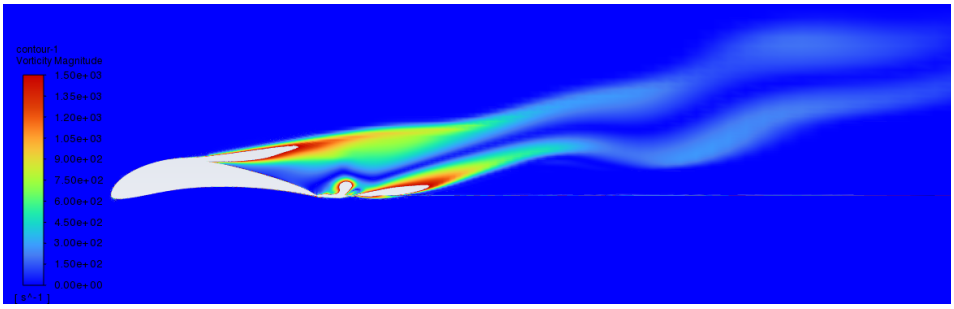

(b) Time = 1s

Figure 6: Vorticity Contours for Unsteady Simulation at AoA 15°

The choice of our time marching scheme showed that our solution will always converge, but care must be taken to ensure that our time scale is smaller than our characteristic time-scale. The choice of time-step was iteratively selected to simulation a $1sec$ flow. A time-step of 0.1 was initally selected but observing random behaviour, the time step was reducedd to 0.01, but the C_L vs time graph was still choppy. Thus, the time-step of 0.01 was selected which resulted in smooth variation of C_L with time and was thus selected.

4 Conclusion

The numerical simulations provide a deeper insight into how the coefficient of lift and drag behave with the increase in the angle of attack of an airfoil. The limitations of the inviscid thin airfoil theory are highlighted as it is unable to capture the viscous effects observed at higher angles of attack or when flow separates. Finally, at higher angles of attack, the flow separation causes vortex shedding

in the wake of the airfoil, drastically increasing the drag experienced by the airfoil.